This is a preprint, the final version is subject to change, of the American Mineralogist (MSA)
Cite as Authors (Year) Title. American Mineralogist, in press.
DOI: https://doi.org/10.2138/am-2020-7284

Revision 1

Reversely zoned plagioclase in lower crustal meta-anorthosites: an indicator of multistage fracturing and metamorphism in the lower crust

YUSUKE SODA[1*], TAKU MATSUDA[1], SACHIO KOBAYASHI[2], MOTOO ITO[2], YUMIKO HARIGANE[3], AND TAKAMOTO OKUDAIRA[1]

[1] Department of Geosciences, Osaka City University, Osaka 558-8585, Japan

[2] Kochi Institute for Core Sample Research, Japan Agency for Marine-Earth Science and Technology (JAMSTEC), Kochi 783-8502, Japan

[3] Geological Survey of Japan, National Institute of Advanced Industrial Science and Technology (AIST), Tsukuba 305-8567, Japan

* Corresponding author

Yusuke Soda

e-mail address; soda@sci.osaka-cu.ac.jp

This is a preprint, the final version is subject to change, of the American Mineralogist (MSA)
Cite as Authors (Year) Title. American Mineralogist, in press.
DOI: https://doi.org/10.2138/am-2020-7284

ABSTRACT

This paper describes the formation mechanism of reversely zoned plagioclase, which has been observed frequently in lower crustal shear zones and is indicative of multistage fracturing and metamorphism in the lower crust, by studying the microstructural and chemical characteristics of plagioclase in sparsely fractured anorthosites and anorthositic mylonites from the Eidsfjord shear zone, Langøya, northern Norway. Based on the field relationship between sparsely fractured anorthosite and anorthositic mylonite, the fracturing of anorthosite occurred before the formation of mylonite. In sparsely fractured anorthosites, transgranular fractures are observed; hydration-reaction products, including Na-rich plagioclase, occur within cracks and fractures, suggesting that hydration reactions occurred during or after fracturing. The hydration reactions in sparsely fractured anorthosites are estimated to have occurred at higher-pressure (*P*) amphibolite-facies conditions (~0.9–1.0 GPa and ~550–700 °C). In anorthositic mylonites, which are considered to have initiated by fracturing and subsequent hydration metamorphism at lower-*P* amphibolite-facies conditions (~0.7 GPa and ~600 °C), recrystallized plagioclase grains often show compositional zoning with an Na-rich core and a Ca-rich rim. Because the compositions of metamorphic plagioclase grains in the sparsely fractured anorthosites and those of the Na-rich

cores of the reversely zoned plagioclase in anorthositic mylonites are similar to each other, the Na-rich cores of the matrix plagioclase in the anorthositic mylonites have recrystallized under higher-*P* amphibolite-facies conditions and then been overgrown or replaced by the Ca-rich rims under lower-*P* conditions. Consequently, the reversely zoned plagioclase observed frequently in lower crustal shear zones is an indicator of multistage brittle fracturing and subsequent hydration metamorphism during exhumation, providing information relevant to understanding the deep rupture process caused by repeated seismicity alternating with aseismic creep below the seismogenic zone.

Keywords: Anorthositic mylonite, Plagioclase, Chemical zoning, Oxygen isotopic composition, Fracturing, Lower crust

This is a preprint, the final version is subject to change, of the American Mineralogist (MSA)
Cite as Authors (Year) Title. American Mineralogist, in press.
DOI: https://doi.org/10.2138/am-2020-7284

INTRODUCTION

Major earthquakes, which nucleate in the seismogenic zone, can cause faults to propagate well into the underlying ductile region at the stage of coseismic displacement (e.g., Ellis and Stöckhert 2004; Jiang and Lapusta 2016). This is predicted to create short-term, high-differential stresses; high strain rates; and related changes of pore fluid pressure in the ductile region near the tip of a seismically active fault in the lower crust. Fracturing in the lower crust may also increase, at least transiently, the permeability of the damaged rock, thus leading to episodic fluid flow into the damaged rock. Such fluid flow would enhance the formation of hydration-reaction products within the damaged rock (e.g., Jamtveit et al. 2018a). These processes may be recorded as microstructures characterized by initial brittle fracturing followed by hydration metamorphism and viscous deformation in lower crustal shear zones (e.g., Svahnberg and Piazolo 2010; Moecher and Steltenpohl 2011; Mukai et al. 2014; Okudaira et al. 2015, 2017; Leib et al. 2016; Menegon et al. 2017; Petley-Ragan et al. 2018; Jamtveit et al. 2019). Understanding the deep ruptures below the seismogenic zone is important for evaluating the recurrence of major earthquakes in the continental crust (Jiang and Lapusta 2016). The microstructures provide information relevant to understanding the deep rupture process caused by repeated seismicity

alternating with aseismic creep below the seismogenic zone.

Variably deformed anorthositic or gabbroic rocks in Langøya, Vesterålen, northern Norway, provide a rare opportunity to study deformation and metamorphic processes in the lower crust. Based on microstructural analyses of plagioclase in anorthositic protomylonites, Okudaira et al. (2017) discussed the roles of fracturing and grain-size-sensitive creep during initiation of the ductile shear zone in meta-anorthosite. Soda and Okudaira (2018) described on microstructures indicative of pulverization in some anorthositic mylonites, which possibly results from stress waves with high stress or strain-rate loadings released by a rupturing fault (e.g., Aben et al. 2016). The reversely zoned plagioclase consisting of Na-rich and Ca-rich domains has been reported in strongly deformed anorthosites (i.e., anorthositic mylonites) formed at the uppermost ductile region of the lower crust (Okudaira et al. 2017; Soda and Okudaira 2018). The reversely zoned plagioclase in the granulite-facies anorthosites and anorthositic gabbros of the Bergen Arcs, western Norway, has been attributed to the breakdown of intermediate plagioclase (with an anorthite mole fraction X_{An} = ~0.5) to a complex intergrowth of Na-rich and Ca-rich domains that developed through phase separation or exsolution, e.g., the Bøggild miscibility gap (Carpenter 1994; Jin and Xu 2017), associated with fluid infiltration into the granulites (Mukai et al. 2014).

However, Petley-Ragan et al. (2018) concluded that the reversely zoned plagioclase can result from the multistage metamorphism under lower crustal conditions.

This study clarifies the formation of reversely zoned plagioclase developed under lower crustal conditions through analysis of the microstructural and chemical characteristics of plagioclase in anorthositic mylonites and sparsely fractured anorthosites. We focused on (1) the pressure (*P*)–temperature (*T*) conditions for fracturing and metamorphism in the sparsely fractured anorthosites in order to reveal the metamorphic history of the Eidsfjord shear zone; (2) major chemical components, crystallographic orientations, and oxygen isotopic compositions ($\delta^{18}O$) in the reversely zoned plagioclase from the anorthositic mylonites in order to reveal the growth history of the reversely zoned plagioclase.

GEOLOGICAL SETTING AND CHARACTERISTICS OF SAMPLES

Anorthositic mylonites and sparsely fractured anorthosites were sampled from Langøya, northern Norway (Fig. 1), anorthosite, mangerite, monzonite, and granitic migmatite underwent upper-amphibolite and granulite-facies metamorphism at 1.8–1.7 Ga (e.g., Griffin et al. 1978; Markl 1998; Plattner et al. 2003; Corfu 2004; Moecher and Steltenpohl 2011), although igneous

textures are well preserved. The Eidsfjord shear zone is a 200-m-thick mylonite zone indicative of top-down-to-the-west normal-slip displacement (Moecher and Steltenpohl 2011) and exhibiting evidence of Caledonian metamorphism and deformation (Klein et al. 1999; Plattner et al. 2003; Steltenpohl et al. 2004, 2011; Moecher and Steltenpohl 2011). The main detachment fault of the Eidsfjord shear zone is exposed at Slåttnes and Grønning (Fig. 1). The hanging wall is composed mainly of coarse-grained, pyroxene-bearing anorthosite. Massive "igneous" gray anorthosite in which tectonic fabrics are not visible at the outcrop scale gradually transitions into bleached white gneissic–mylonitic meta-anorthosite toward the shear zone (Markl 1998; Moecher and Steltenpohl 2011). The anorthosite contains plagioclase laths up to 3 cm long with variable amounts of interstitial pyroxene and Fe–Ti oxides (Markl 1998). The footwall consists of coarse-grained, light-gray, biotite-bearing monzonite, and ferrodiorite, grading into mylonite in the detachment zone. Pseudotachylyte occurs throughout the shear zone (Løseth and Tveten 1996; Markl 1998; Plattner et al. 2003; Moecher and Steltenpohl 2011; Steltenpohl et al. 2011). Pseudotachylyte crosscuts the mylonite foliation and includes angular clasts of anorthositic mylonite, suggesting alternating periods of pseudotachylyte formation and mylonitization (Moecher and Steltenpohl 2011). The *P–T* conditions reached by the metamorphosed

pseudotachylyte and meta-anorthosite are estimated to be ~0.6–0.7 GPa and ~600–700 °C based on garnet–hornblende–plagioclase–quartz geothermobarometry (Moecher and Steltenpohl 2011; Leib et al. 2016; Okudaira et al. 2017). Ar–Ar laser incremental heating analyses gave $^{40}Ar/^{39}Ar$ plateau ages for the muscovite-bearing anorthositic ultramylonites of 403.6 ± 1.1 Ma (Steltenpohl et al. 2011), interpreted to represent the age of crystallization during the main fabric-forming deformation in the Eidsfjord detachment.

The sparsely fractured anorthosites occur everywhere in the hanging wall of the Eidsfjord detachment. The mylonite zone is narrow (<3 m wide) and developed within the sparsely fractured anorthosites at sharp contacts with no distinct strain gradient. Tectonic foliation and lineation are developed in the anorthositic mylonites, not in the surrounding sparsely fractured anorthosites. In this study, anorthositic mylonite (sample 160730-02) in Fleinnes and sparsely fractured anorthosite (sample 170731-02) in Kjørstad were analyzed (Fig. 1b). The sparsely fractured anorthosite sample was collected ~1 m away from the anorthositic mylonite zone. Mineral abbreviations follow Whitney and Evans (2010).

ANALYTICAL METHODS

Chemical compositions of minerals were determined with an electron microprobe (JEOL JXA-8800) at Osaka City University (15 kV accelerating voltage, 20 nA beam current, and 3 μm beam diameter). Raw counts from characteristic X-ray peaks for nine elements were converted to weight percent oxides compared with natural and synthetic standards using the ZAF correction method.

We analyzed the crystallographic orientations of the plagioclase grains using a scanning electron microscope (SU3500, Hitachi) equipped with an electron backscatter diffraction (EBSD) system (HKL NordlysNano, Oxford Instruments) and AZtec Software at the Geological Survey of Japan, National Institute of Advanced Industrial Science and Technology (AIST). Thin sections of the anorthositic mylonites were cut perpendicular to the mylonitic foliation and parallel to the stretching lineation. Before scanning electron microscopy (SEM) analysis, surface damage was removed from the thin sections through several minutes of treatment with a vibratory polisher (VibroMet2, Buehler) using colloidal silica. EBSD measurement was conducted under an accelerating voltage of 15 kV, a working distance of 15–20 mm, specimen tilting to 70°, and the low-vacuum mode. EBSD data were obtained using automatic indexing with a step size of 1–5 μm. We used the Matlab toolbox MTEX version 4.5 (Mainprice et al.

2014) to analyze the EBSD data.

We conducted oxygen isotope measurements of polished thin sections of the samples and appropriate mineral standards with an AMETEK CAMECA ims-6F secondary ion mass spectrometer (SIMS) at the Kochi Institute for Core Sample Research, Japan Agency for Marine-Earth Science and Technology (JAMSTEC). To remove electrostatic charging during analysis, the sample surface was coated with a thin carbon film. The primary ions were mass-filtered $^{133}Cs^{+}$ accelerated to 14.5 keV, and the beam had an ~10-μm-diameter spot size. An electron gun was used for charge compensation of the analysis area. Negative secondary ions of 15.9 amu, ^{16}O, ^{18}O, and ^{30}Si were acquired sequentially in peak-switching mode with a combination of a Faraday cup (FC) and an electron multiplier (EM) at a mass resolving power of approximately 4,000, sufficient to distinguish the relevant isobaric interferences (^{18}O peak from $^{1}H_2{}^{16}O$ peak and ^{30}Si peak from $^{29}Si^{1}H$ peak). Each measurement consists of 30 cycles of 15.9 amu for 1 s (FC), ^{16}O for 1 s (FC), ^{18}O for 1 s (EM), and ^{30}Si for 1 s (EM). Each run started after stabilization of the secondary ion beam following presputtering for 70 s. The total acquisition time for each analysis was 258 s, including waiting time and the presputtering process. Miyake-jima anorthite ($\delta^{18}O_{VSMOW}$ = +5.2‰) and Virginia albite ($\delta^{18}O_{VSMOW}$ = +10.4‰) were

used as standards to correct for instrumental mass fractionation. Under these analytical conditions, the matrix effect is mostly correlated with the anorthite–albite compositions of plagioclase feldspar (O'Neil and Taylor 1967). Although calibration based on Miyake-jima anorthite was performed for various anorthite–albite compositions in the thin section, variations in the matrix effect among these compositional minerals were ~±4‰ (1σ). The reproducibility of $\delta^{18}O_{VSMOW}$ on different analyses of these standards was within ~2‰ (1σ).

RESULTS

Microstructures in the sparsely fractured anorthosites

The sparsely fractured anorthosites consist mainly of plagioclase and orthopyroxene (Fig. 2a). Orthopyroxene occurs as an interstitial phase with weakly kinked cleavages. Clinopyroxene is observed only as an exsolution phase along orthopyroxene cleavage planes or rims. Coarse-grained plagioclase exhibits mechanical twins (e.g., Albite or Pericline twins), deformation bands, cracks, and zones with fine-grained plagioclase. The mechanical twins showing tapering and bent shapes (Fig. 2b) are offset or terminated by cracks. Within some cracks, fine-grained (<10 μm) plagioclase is observed (Figs. 2b and 2c). Zones of fine-grained

plagioclase grains develop as transgranular fractures and occasionally transform into cracks at the tip, suggesting that they were related to brittle fracturing (i.e., fracture zones). The X_{An} of coarse-grained intact plagioclases ranges from 0.44 to 0.76 (Fig. 3). Fine-grained plagioclases in the cracks are more sodic (Fig. 3), and the 1σ ranges of X_{An} are 0.25–0.43. Low-X_{An} fine-grained plagioclase precipitated with epidote, kyanite, and quartz in crack-related spaces in coarse-grained plagioclase (Figs. 2d and 2e).

Cummingtonite + tschermakite-pargasite hydration-reaction products develop between orthopyroxene and plagioclase grains (Fig. 2f), suggesting the incomplete breakdown of plagioclase and orthopyroxene because of a limited supply of H_2O (Austrheim and Robins 1981). The chemical composition of the cummingtonite is Si = 7.91–8.00; X_{Mg} = 0.63–0.67; $(Na + K)_A$ ≤0.04, where O = 23. Tschermakite and pargasite occur as an aggregate of fibrous grains with fibrous biotite (Figs. 2c and 2f). Tschermakite and pargasite also occur within cracks in coarse-grained plagioclase. The chemical compositions of tschermakite and pargasite are Si = 6.05–6.34; X_{Mg} = 0.52–0.61; $(Na + K)_A$ = 0.33–0.50 and Si = 6.07–6.26; X_{Mg} = 0.48–0.57; $(Na + K)_A$ = 0.51–0.62, respectively (Supplemental Fig. S1). The tschermakite-pargasite aggregates are occasionally replaced by hornblende and actinolite (Fig. 2f), suggesting that the sequential

This is a preprint, the final version is subject to change, of the American Mineralogist (MSA)
Cite as Authors (Year) Title. American Mineralogist, in press.
DOI: https://doi.org/10.2138/am-2020-7284

formation of tschermakite-pargasite and hornblende–actinolite during retrogression. Although the chemical compositions of the amphiboles are homogeneous within a single grain, they vary even within a single thin section (Supplemental Fig. S1). Garnet occurs in the tschermakite-pargasite and biotite aggregate (Fig. 2f), not within the cummingtonite aggregate. Garnet grains are euhedral to subhedral and exhibit no distinct compositional zoning (Supplemental Fig. S2). The 1σ range values of X_{Alm}, X_{Grs}, and X_{Prp} at the core and the rim are 0.62–0.66 (core) and 0.63–0.67 (rim), 0.14–0.17 (core) and 0.13–0.16 (rim), and 0.18–0.23 (core) and 0.18–0.23 (rim), respectively.

Microstructures in the anorthositic mylonites

The anorthositic mylonites consist mainly of plagioclase, epidote, amphibole, muscovite, and biotite (Fig. 4), with minor amounts of garnet, quartz, scapolite, Fe–Ti oxides, kyanite, K-feldspar, and apatite. As Figure 4a shows, plagioclase occurs as a recrystallized matrix (~0.2 mm in diameter) and porphyroclasts (~2–5 mm in diameter). Plagioclase grains forming the matrix exhibit an equilibrium structure (i.e., a foam structure) with straight grain boundaries and triple junctions with dihedral angles of ~120° (Fig. 4b). Such plagioclase grains occasionally contain

fine-grained epidote inclusions. Some matrix plagioclase grains are optically zoned, and the zonal structure is not always concentrically developed in a grain (Fig. 4b).

Figures 5a and 5b indicate that the core and rim of optically zoned plagioclase correspond to the Na-rich and Ca-rich areas in the elemental map, respectively. Figure 5c shows a map of the intragranular misorientation between a given point and the average orientation (MTEX toolbox "mis2mean"). Slight crystallographic orientation differences, shown as a subtle color change from blue to deep blue on the map, are observed in the plagioclase grains, but they do not coincide with the optically and chemically defined core and rim. A line profile of differences in crystallographic orientation also shows a low degree of misorientation regardless of the zonal structure (Fig. 5d), indicating that the difference in optic orientation between the core and rim reflects the difference in chemical composition. There are no microscopic pores in rims and cores under SEM observations.

Figure 6 shows the compositional variation of plagioclase cores, rims, and porphyroclasts. The variation (1σ range) in plagioclase composition (X_{An}) for cores, rims, and porphyroclasts are 0.26–0.36, 0.39–0.45, and 0.36–0.43, respectively. The compositional variation of the Na-rich cores is comparable to that of the low-X_{An} crack-infilling plagioclase in the sparsely fractured

This is a preprint, the final version is subject to change, of the American Mineralogist (MSA)
Cite as Authors (Year) Title. American Mineralogist, in press.
DOI: https://doi.org/10.2138/am-2020-7284

anorthosites (Figs. 3 and 6), whereas the compositional variation of the porphyroclasts is similar to that of the Ca-rich rims.

Oxygen isotopic compositions for plagioclase in the anorthositic mylonites

We measured $\delta^{18}O_{VSMOW}$ of the Na-rich cores and Ca-rich rims of six chemically zoned plagioclase grains in the anorthositic mylonites by way of spot analysis with SIMS. The mean values for $\delta^{18}O_{VSMOW}$ are 5.6 ± 3.5‰ for Na-rich cores and 5.2 ± 3.4‰ for Ca-rich rims (Supplemental Table S1). As shown in Figure 7a, their values of $\delta^{18}O_{VSMOW}$ do not form distinct groupings. The values of $\delta^{18}O_{VSMOW}$ within each grain (the results for Grain 6 are shown in Fig. 7b) are relativity uniform (+7 to +11‰) in the rim, but they vary more widely in the core (+4 to +12‰). However, considering the measurement errors, there is no significant difference between the values of $\delta^{18}O_{VSMOW}$ of the Na-rich core and those of the Ca-rich rim of a single grain.

DISCUSSION

Pressure–temperature–fluid conditions at the time of fracturing and subsequent fluid infiltration in the sparsely fractured anorthosites

This is a preprint, the final version is subject to change, of the American Mineralogist (MSA)
Cite as Authors (Year) Title. American Mineralogist, in press.
DOI: https://doi.org/10.2138/am-2020-7284

In the sparsely fractured anorthosites, the low-X_{An} fine-grained plagioclase occurs with epidote, kyanite, and quartz in the crack-related spaces in coarse-grained plagioclase (Figs. 2d and 2e). Difference in chemical composition between the coarse-grained intact plagioclase and the crack-infilling fine-grained plagioclase (Fig. 3) suggests that the sodic fine grains were formed by metamorphic crystallization. The aggregates of tschermakite and pargasite grains are replaced by hornblende and actinolite (Fig. 2f), suggesting that hornblende and actinolite were formed during retrogression. Tschermakite and pargasite are spatially close to the sodic fine-grained plagioclase and garnet (Figs. 2c and 2d). Based on these observations, the low-X_{An} fine-grained plagioclase, tschermakite-pargasite, epidote, garnet, kyanite, and quartz may coexist in equilibrium during hydration metamorphism.

These recrystallized minerals are confined to the vicinity of fractures rather than occurring throughout the sparsely fractured anorthosite. This observation indicates that overall chemical equilibrium was not attained and the bulk-rock compositions are not equal to the composition of effective reaction volume. Because the effective bulk compositions are difficult to evaluate, we applied conventional geothermobarometry, rather than pseudosection analysis, to estimate *P–T* conditions at the time of fracturing and subsequent fluid infiltration. Based on the mineral

chemistry of the recrystallized plagioclase, tschermakite-pargasite, and garnet in the sparsely fractured anorthosites, we applied the amphibole–plagioclase NaSi–CaAl exchange thermometer (Holland and Blundy 1994), the garnet–amphibole Fe–Mg exchange thermometer (Ravna 2000), and the garnet–amphibole–plagioclase–quartz barometer (Kohn and Spear 1990) to estimate *P–T* conditions. The typical temperature and pressure uncertainties are ±40 °C, ±90 °C, and ±50 MPa for the three thermobarometers, respectively. Because the tschermakite-pargasite and garnet grains exhibit no distinct compositional zoning (Supplemental Figs. S1 and S2), the core compositions of the garnet and of tschermakite or pargasite near the garnet are used to estimate *P–T* conditions. Plagioclases used for the calculations are crack-infilling plagioclases, which are spatially closest to tschermakite-pargasite and garnet. The amphibole formulas were recalculated using the calculation schemes of each thermobarometer. Table 1 lists the results of our *P–T* estimates for five pairs of plagioclase + tschermakite-pargasite + garnet. The temperatures are calculated to be 545–687 °C at 900 MPa, and the pressures are 856–1011 MPa at 600 °C. Figure 8 summarizes the *P–T* estimates. The intersections between the isopleths calculated by the three thermobarometers for each pair plot appear close together, especially for pairs 2 and 5, suggesting that these are geologically meaningful *P–T* estimates. As a result, the pressure and temperature

ranges for hydration in the sparsely fractured anorthosites are ~0.9–1.0 GPa and ~550–700 °C, respectively, consistent with high-*P* amphibolite-facies metamorphism.

The *P*–*T* ranges of the sparsely fractured anorthosites are comparable to the *P*–*T* conditions (1.1 ± 0.2 GPa, ~650 °C) for garnet-bearing mineral assemblages in mylonitic gneisses associated with mylonitic pseudotachylyte and in metamorphosed pseudotachylyte from the Fiskfjord shear zone, closely related to the Eidsfjord shear zone (Leib et al. 2016). However, the pressure range of hydration in the sparsely fractured anorthosites (1.1 ± 0.2 GPa) is higher than that in anorthositic mylonites in the Eidsfjord shear zone (~0.6–0.7 GPa: Moecher and Steltenpohl 2011; Leib et al. 2016; Okudaira et al. 2017). This disparity implies that hydration metamorphism occurred, at least twice, in the Eidsfjord shear zone. The mylonite zone is developed within the sparsely fractured anorthosite, and tectonic foliation and lineation are developed only in the anorthositic mylonites, not in the surrounding sparsely fractured anorthosites, implying that the mylonite formation occurred after the fracturing of anorthosites. The lower-*P* metamorphism can be interpreted to have occurred after the higher-*P* metamorphism in the Eidsfjord shear zone.

Jamtveit et al. (2018b) suggested that the pressure experienced by the Caledonian eclogite-facies metamorphism in the Proterozoic granulites of the Bergen Arcs is not uniquely

related to its depth of burial, since the development of a weak shear zone within a stressed lower crust can generate a significant pressure increase inside the shear zone as the corresponding differential stresses (Schmalholz and Podladchikov 2013; Moulas et al. 2014). Because the sparsely fractured anorthosites could not be deformed ductilely and then would not develop as a weak shear zone, the higher-*P* metamorphism recorded in microstructures caused by local fracturing was related not to a local pressure perturbation but to deeper (i.e., a ~32- to 35-km depth, assuming a rock density of 2900 kg/m^3) fracturing and metamorphism.

Scapolite is hardly observed in the sparsely fractured anorthosites, whereas it occurs ubiquitously in the anorthositic mylonites, suggesting that fluid composition was not rich in CO_2 during the higher-*P* amphibolite-facies metamorphism but rich in CO_2 during the lower-*P* amphibolite-facies metamorphism (e.g., Moecher and Essene 1991; Lamb and Moecher 1992). The chlorine content in amphiboles is also different between the sparsely fractured anorthosite and the anorthositic mylonite; the former is not detectable and the latter is ~0.3 wt% (table 2 of Okudaira et al. 2017). These results suggest that fluid compositions related to the first-stage higher-*P* and the second-stage lower-*P* amphibolite-facies metamorphisms were different at least in CO_2 and Cl contents.

This is a preprint, the final version is subject to change, of the American Mineralogist (MSA)
Cite as Authors (Year) Title. American Mineralogist, in press.
DOI: https://doi.org/10.2138/am-2020-7284

Formation of the reversely zoned plagioclase

Mukai et al. (2014) suggested that a plagioclase miscibility gap at intermediate compositions (i.e., Bøggild gap) should exsolve to two-phase intergrowth of Na-rich and Ca-rich domains and that the introduction of fluid, aided by stress, could recrystallize and coarsen the nanoscale Bøggild intergrowth thus formed into a reversely zoned plagioclase. However, Petley-Ragan et al. (2018) attributed the zonal structure of fine-grained plagioclase to the breakdown below 0.8 GPa of Na-rich plagioclase formed at high pressures to Ca-rich plagioclase, based on the results of thermodynamic analyses by Wayte et al. (1989) and Wain et al. (2001).

In the anorthositic mylonites, there is no observable variation in the value of $\delta^{18}O_{VSMOW}$ from the core to the rim of the matrix plagioclase grains (Fig. 7). This implies phase separation or exsolution of intermediate plagioclase with a homogeneous value of $\delta^{18}O_{VSMOW}$. However, in the reversely zoned plagioclase grains analyzed here, the chemical compositions of the Na-rich cores and Ca-rich rims are not consistent with the Bøggild gap (Fig. 9a). Variations in $\delta^{18}O_{VSMOW}$ within a single crystal are controlled mainly by the value of $\delta^{18}O_{VSMOW}$ of the fluid in equilibrium with the surface of a growing plagioclase grain and by O-volume diffusion (e.g., O'Neil and

Taylor 1967; Sharp and Moecher 1994). Isotopic exchange experiments with anhydrous fluid (O_2 or CO_2) obtain diffusion rates of oxygen in plagioclase that are orders of magnitude slower than those obtained for exchange with hydrous fluid (Elphick et al. 1988). Oxygen diffusion coefficients in anorthite under hydrothermal conditions (i.e., wet values, preexponential factor D_0 = 1.4 × 10^{-11} m^2/s, and activation energy for diffusion E = 110 kJ/mol; Giletti et al. 1978) are orders of magnitude higher than equivalent dry values (D_0 = 1.0 × 10^{-9} m^2/s and E = 236 kJ/mol; Elphick et al. 1988) at similar temperatures. Given an initial difference in values of $\delta^{18}O_{VSMOW}$ with 20‰, comparable to the difference between the highest and the lowest values of $\delta^{18}O_{VSMOW}$ values in the samples analyzed here, the relaxation time for isotopic diffusion at 600 °C for a 200-μm-radius plagioclase grain can be evaluated by using the diffusion equation for a sphere of Crank (1975). Such calculations indicate that exchange of plagioclase would occur with a hydrous fluid in several thousand years but that the original values of $\delta^{18}O_{VSMOW}$ would be retained in the cores for hundreds of millions of years if exchange occurred with an anhydrous fluid. In the anorthositic mylonites, hydrous or CO_2-bearing phases (e.g., amphibole, mica, epidote, and scapolite) have been ubiquitously observed between plagioclase grains, suggesting the presence of an H_2O- and CO_2-bearing fluid at grain boundaries, at least at the time of

mylonite formation. Although we cannot evaluate the actual values of the oxygen diffusion coefficient in anorthite with the H_2O- and CO_2-bearing fluid, the diffusion rate of oxygen is faster than that with an anhydrous fluid. Therefore, even if the variations of $\delta^{18}O_{VSMOW}$ developed because of changes in fluid composition during the growth of plagioclase, oxygen isotopic exchange with the H_2O- and CO_2-bearing fluid and diffusion would likely have obliterated the variations of $\delta^{18}O_{VSMOW}$ in the plagioclase.

Cole (2000) and Fiebig and Hoefs (2002) suggested that oxygen isotopic exchange between minerals and surrounding hydrothermal fluids is controlled largely by surface reactions such as dissolution–reprecipitation. When the dissolving parent phase and the new product phase are in contact and the reaction is interface controlled, the interface control must be responsible for the transfer of crystallographic information, such as crystallographic orientation, from parent to product, as epitaxy is common in many replacement reactions (Putnis 2002; Plümper et al. 2017). In the anorthositic mylonites, there is no difference between the crystallographic orientation of the Na-rich core and that of the Ca-rich rim in a single plagioclase grain (Fig. 5). This implies that dissolution–reprecipitation or replacement reactions occurred at Na-rich plagioclase–fluid interfaces resulting in the formation of Ca-rich rims, but based on our SEM observations

This is a preprint, the final version is subject to change, of the American Mineralogist (MSA)
Cite as Authors (Year) Title. American Mineralogist, in press.
DOI: https://doi.org/10.2138/am-2020-7284

microscale porosity, which is typically interpreted to be resulted from fluid-mediated replacement reactions (Putnis 2015; Plümper et al. 2017; Giuntoli et al. 2018), is lacking in Ca-rich rims (Supplemental Fig. S3).

The breakdown reaction of zoisite + kyanite + quartz + plagioclase at high- and low-pressures would crystallize Na-rich and Ca-rich plagioclase, respectively. As Figure 9b shows, for a plagioclase solid solution, breakdown occurs initially below a pressure of ~1.7 GPa at 600 °C by continuous reaction (Goldsmith 1982; Wayte et al. 1989):

$$\text{zoisite} + \text{kyanite} + \text{quartz} + \text{plagioclase} = (\text{NaSiCa}_{-1}\text{Al}_{-1})_{\text{Pl}} + \text{H}_2\text{O} \quad (1)$$

This reaction proceeds to the right with decreasing pressure and/or increasing temperature (Goldsmith 1982; Wayte et al. 1989; Wain et al. 2001). Based on the simple mass balance calculation, breakdown of 1 mole of plagioclase of X_{An} = 0.5 would produce 0.206 mole of zoisite + 0.034 mole of kyanite + 0.017 mole of quartz + 0.744 mole of plagioclase of X_{An} = 0.3, resulting in a modal ratio of epidote to plagioclase of 0.28:1. In the sparsely fractured anorthosite, some cracks filled with fine-grained plagioclase, epidote, and kyanite, and quartz exhibit modal

ratios of epidote to plagioclase (X_{An} = ~0.2–0.4) of ~0.2–0.4:1, indicating that modal abundance of plagioclase and epidote can be explained by the reaction (1). However, in the anorthositic mylonite, the modal ratio of epidote to plagioclase is ~0.2–0.3:1, and it is not consistent with the result of the mass balance calculation giving the breakdown of plagioclase (X_{An} = 0.3) + epidote + kyanite + quartz to produce plagioclase of X_{An} = 0.4. Breakdown of 80% plagioclase of X_{An} = 0.3 would result in a modal ratio of zoisite to plagioclase of 0.13:1. In the anorthositic mylonites, scapolite is ubiquitously observed at grain boundaries between plagioclase grains, and some plagioclase grains may be consumed by the scapolite-forming reactions in the presence of CO_2-bearing fluid, which would result in the modal abundance of plagioclase less than the estimated by the simple mass balance calculation.

Based on the similarity between the X_{An} values of low-X_{An} plagioclase grains in the sparsely fractured anorthosites and those of the cores of the reversely zoned plagioclase in the anorthositic mylonites (Figs. 3 and 6), the Na-rich cores of the matrix plagioclase recrystallized at the first-stage higher-P metamorphism of ~0.9–1.0 GPa and ~550–700 °C. Then, the Ca-rich rims were overgrown or replaced at the second-stage lower-P metamorphism of ~0.6–0.7 GPa at ~600–700 °C. In the P–X_{An} phase diagram (Fig. 9b), the compositional ranges of the Na-rich

cores and Ca-rich rims and their relevant pressure ranges are comparable with the equilibrium phase boundaries for 500 and 600 °C, suggesting that the compositional difference between the Na-rich cores and the Ca-rich rims of the reversely zoned plagioclase can be explained by the pressure difference between the first-stage higher-*P* and the second-stage lower-*P* metamorphisms. This implies that the zonal structure of the matrix plagioclase grains in the anorthositic mylonites resulted from two-stage growth of plagioclase during nearly isothermal decompression. The early-stage higher-*P* deformation microstructures and metamorphic features in the anorthositic mylonites were obliterated or partially modified by the later-stage lower-*P* deformation and metamorphism. In sparsely fractured anorthosites, some fine-grained plagioclase grains in transgranular fracture zones within coarse-grained plagioclase exhibit compositional zoning comparable to that developed in the mylonites, suggesting that the second-stage lower-*P* hydration metamorphism (i.e., the mylonite-forming stage) occurred locally in the sparsely fractured anorthosites.

IMPLICATIONS

Fracturing in the lower crust may increase, at least transiently, the permeability of the

damaged rock, thus leading to episodic fluid flow into the damaged rock, and such fluid flow would enhance the formation of hydration-reaction products within the damaged rock (e.g., Jamtveit et al. 2018a, b). Because these processes may be recorded as microstructures characterized by initial brittle fracturing followed by hydration metamorphism and viscous deformation in lower crustal shear zones, the microstructures provide us with information for understanding the deep rupture process caused by repeated co-seismic rupture alternating with aseismic creep below the seismogenic zone. We advocate that the reversely zoned plagioclase that has been observed frequently in lower crustal shear zones is a characteristic microstructure indicating multistage brittle fracturing and subsequent hydration metamorphism during exhumation.

In the sparsely fractured anorthosites, hydration-reaction products, including sodic plagioclase, occur within cracks, suggesting that hydration reactions occurred under the conditions of higher-*P* amphibolite facies (~0.9–1.0 GPa and ~550–700 °C) during or after fracturing (Fig. 10a). In the anorthositic mylonites, brittle fracturing and subsequent hydration metamorphism under conditions of lower-*P* amphibolite facies (~0.6–0.7 GPa and ~600–700 °C) have been reported (Moecher and Steltenpohl 2011; Leib et al. 2016; Okudaira et al. 2017). Thus, in the

Eidsfjord shear zone, brittle deformation, and related hydration metamorphism can be interpreted as having occurred, at least twice, under the different *P–T* conditions (Fig. 10b).

Because the X_{An} values of low-X_{An} plagioclase grains in the sparsely fractured anorthosites and those of the cores of the reversely zoned plagioclase in the anorthositic mylonites are similar to each other, the Na-rich cores of the matrix plagioclase grains in the anorthositic mylonites recrystallized under higher-*P* amphibolite-facies conditions (Fig. 10a). The sodic cores of the matrix plagioclase grains were then overgrown or replaced by the Ca-rich rims under lower-*P* amphibolite facies (Fig. 10b). The lack of a difference between the values of $\delta^{18}O_{VSMOW}$ of the cores and those of the rims may have resulted from isotopic homogenization via diffusional modification through intergranular fluid. Although the later-stage episodic fluid flow into the sparsely fractured anorthosites led to metamorphic modification on microstructures and chemical compositions of constituent minerals formed at early-stage fracturing and metamorphism, the evidence for early-stage fracturing and metamorphism has been preserved as the reversely zoned plagioclase in the anorthositic mylonites. Consequently, reversely zoned plagioclase observed frequently in lower crustal shear zones is an indicator of multistage brittle fracturing and subsequent hydration metamorphism during exhumation.

FUNDING

TO was supported financially by Japan's Ministry of Education, Culture, Sports, Science and Technology (MEXT) Grants-in-Aid for Scientific Research (KAKENHI) grants 26109004, 16K05613, and 18H01297. MI was partly supported by MEXT KAKENHI grants 18K18795 and 18H04468. This work was supported in part by the Kochi Core Center Open Facility System (KOFS) under the MEXT foundation.

ACKNOWLEDGMENTS

We thank N. Shigematsu for permitting us to use the SEM-EBSD at the Geological Survey of Japan, AIST, and J. Fukuda for fruitful discussion. T. Matsuzaki is thanked for his assistance in accessing the SIMS facility at the Kochi Institute for Core Sample Research, JAMSTEC. Almost all MTEX scripts used in this study were originally written by D. Mainprice. D.P. Moecher, L. Menegon, and an anonymous reviewer are thanked for their constructive comments. D.R. Baker and T. Mueller are appreciated for their editorial handling of this paper.

REFERENCES CITED

Aben, F.M., Doan, M.-L., Mitchell, T.M., Toussaint, R., Reuschlé, T., Fondriest, M., Gratier, J.-P., and Renard, F. (2016) Dynamic fracturing by successive coseismic loadings leads to pulverization in active fault zones. Journal of Geophysical Research: Solid Earth, 121, 2338–2360.

Austrheim, H., and Robins, B. (1981) Reactions involving hydration of orthopyroxene in anorthosite-gabbro. Lithos, 14, 275–281.

Carpenter, M.A. (1994) Subsolidus phase relations of the plagioclase feldspar solid solution. In I. Parsons, Ed., Feldspars and their Reactions, p. 221–269. Kluwer Academic, Dordrecht.

Cole, D.R. (2000) Isotopic exchange in mineral-fluid systems IV. The crystal chemical controls on oxygen isotope exchange rates in carbonate-H_2O and layer silicate-H_2O systems. Geochimica et Cosmochimica Acta, 64, 921–933.

Corfu, F. (2004) U–Pb geochronology of the Leknes Group: an exotic early-Caledonian metasedimentary assemblage stranded on Lofoten basement, northern Norway. Journal of the Geological Society of London, 161, 619–627.

Crank, J. (1975) The Mathematics of Diffusion, 2nd ed., 145 p. Oxford University Press, London.

Ellis, S., and Stöckhert, B. (2004) Elevated stresses and creep rates beneath the brittle–ductile transition caused by seismic faulting in the upper crust. Journal of Geophysical Research: Solid Earth, 109, B05407, doi:10.1029/2003JB002744.

Elphick, S.C., Graham, C.M., and Dennis, P.F. (1988) An ion microprobe study of anhydrous oxygen diffusion in anorthite: a comparison with hydrothermal data and some geological implications. Contributions to Mineralogy and Petrology, 100, 490–495.

Fiebig, J., and Hoefs, J. (2002) Hydrothermal alteration of biotite and plagioclase as inferred from intra- granular oxygen isotope- and cation-distribution patterns. European Journal of Mineralogy, 14, 49–60.

Giletti, B.J., Semet, M.P., and Yund, R.A. (1978) Studies in diffusion–III. Oxygen in feldspars: an ion microprobe determination. Geochimica et Cosmochimica Acta, 42, 45–57.

Giuntoli, F., Menegon, L., and Warren, C.J. (2018) Replacement reactions and deformation by dissolution and precipitation processes in amphibolites. Journal of Metamorphic Geology, 36, 1263–1286.

Goldsmith, J.R. (1982) Plagioclase stability at elevated temperatures and water pressures. American Mineralogist, 67, 653–675.

Griffin, W.L., Tayor, P.N., Hakkinen, J.W., Heier, K.S., Iden, I.K., Krogh, E.J., Malm, O., Olsen, K.I., Ormaasen, D.E., and Tveten, E. (1978) Archean and Proterozoic crustal evolution in Lofoten-Vesterålen, N Norway. Journal of Geological Society of London, 135, 629–647.

Holdaway, M.J. (1971) Stability of andalusite and the aluminum silicate phase diagram. American Journal of Science, 271, 97–131.

Holland, T., and Blundy, J. (1994) Non-ideal interactions in calcic amphiboles and their bearing on amphibole-plagioclase thermometry. Contributions to Mineralogy and Petrology, 116, 433–447.

Holland, T.J.B., and Powell, R. (1998) An internally consistent thermodynamic data set for phases of petrological interest. Journal of Metamorphic Geology, 16, 309–343.

Jamtveit, B., Ben-Zion, Y., Renard, F., and Austrheim, H. (2018a) Earthquake-induced transformation of the lower crust. Nature, 556, 487–491.

Jamtveit, B., Moulas, E., Andersen, T.B., Austrheim, H., Corfu, F., Petley-Ragan, A., and Schmalholz, S.M. (2018b) High pressure metamorphism caused by fluid induced weakening of deep continental crust. Scientific Reports, 8, 17011, doi:10.1038/s41598-018-35200-1.

Jamtveit, B., Petley-Ragan, A., Incel, S., Dunkel, K.G., Aupart, C., Austrheim, H., Corfu, F.,

Menegon, L., and Renard, F. (2019) The effects of earthquakes and fluids on the metamorphism of the lower continental crust. Journal of Geophysical Research: Solid Earth, 124, 7725–7755.

Jiang, J., and Lapusta, N. (2016) Deeper penetration of large earthquakes on seismically quiescent faults. Science, 352, 1293–1294.

Jin, S., and Xu, H. (2017) Study on structure variations of incommensurately modulated labradorite feldspars with different cooling histories. American Mineralogist, 102, 1328–1339.

Klein, A.C., Steltenpohl, M.G., Hames, W.G., and Andresen, A. (1999) Ductile and brittle extension in the southern Lofoten archipelago, north Norway: implications for differences in tectonic style along ancient collisional margin. American Journal of Science, 299, 69–89.

Kohn, M.J., and Spear, F.S. (1990) Two new geobarometers for garnet amphibolites, with applications to southeastern Vermont. American Mineralogist, 75, 89–96.

Lamb, W.M., and Moecher, D.P. (1992) CO_2-rich fluid inclusions in the Whitestone Anorthosite: implications for the retrograde history of the Parry Sound Shear Zone, Grenville Province, Canada. Journal of Metamorphic Geology, 10, 763–776.

Leake, B.E., Woolley, A.R., Arps, C.E.S., Birch, W.D., Gilbert, M.C., Grice, J.D., Hawthorne,

F.C., Kato, A., Kisch, H.J., Krivovichev, V.G., and others (1997) Nomenclature of amphiboles: Report of the Subcommittee on amphiboles in the International Mineralogical Association, Commission on new minerals and mineral names. Canadian Mineralogist, 35, 219–246.

Leib, S.E., Moecher, D.P., Steltenpohl, M.G., and Andresen, A. (2016) Thermobarometry of metamorphosed pseudotachylyte and associated mylonite: Constraints on dynamic co-seismic rupture depth attending Caledonian extension, North Norway. Tectonophysics, 682, 85–95.

Løseth, H., and Tveten, E. (1996) Post-Caledonian structural evolution of the Lofoten and Vesterålen offshore and onshore areas. Norsk Geologisk Tidsskrift, 76, 215–230.

Mainprice, D., Bachmann, F., Hielscher, R., and Schaeben, H. (2014) Descriptive tools for the analysis of texture projects with large datasets using MTEX: strength, symmetry and components. In D.R. Faulkner, E. Mariani, and J. Mecklenburgh, Eds., Rock Deformation from Field, Experiments, and Theory: A Volume in Honour of Ernie Rutter, Geological Society of London, Special Publication, 409, 223–249.

Markl, G. (1998) The Eidsfjord anorthosite, Vesterålen, Norway: field observations and geochemical data. Norges Geologiske Undersøkelse Bulletin, 434, 53–75.

Menegon, L., Pennacchioni, G., Malaspina, N., Harris, K., and Wood, E. (2017) Earthquakes as

precursors of ductile shear zones in the dry and strong lower crust. Geochemistry, Geophysics, Geosystems, 18, 4356–4374.

Moecher, D.P., and Essene, E.J. (1991) Calculation of CO_2 activities using scapolite equilibria: constraints on the pressure and composition of a fluid phase during high grade metamorphism. Contributions to Mineralogy and Petrology, 108, 219–240.

Moecher, D.P., and Steltenpohl, M.G. (2011) Petrological evidence for co-seismic slip in extending middle-lower continental crust: Heier's zone of pseudotachylyte, north Norway. In Å. Fagereng, V. Toy, and J.V. Rowland, Eds., Geology of the Earthquake Source: A Volume in Honour of Rick Sibson, Geological Society of London, Special Publication, 359, 169–186.

Moulas, E., Burg, J.-P., and Podladchikov, Y. (2014) Stress field associated with elliptical inclusions in a deforming matrix: Mathematical model and implications for tectonic overpressure in the lithosphere. Tectonophysics, 631, 37–49.

Mukai, H., Austrheim, H., Putnis, C.V., and Putnis, A. (2014) Textural evolution of plagioclase feldspar across a shear zone: Implications for deformation mechanism and rock strength. Journal of Petrology, 55, 1457–1477.

Newton, R.C., Charlu, T.V., and Kleppa, O.J. (1980) Thermochemistry of the high structural state

plagioclases. Geochimica et Cosmochimica Acta, 44, 933–941.

Okudaira, T., Jeřábek, P., Stünitz, H., and Fusseis, F. (2015) High-temperature fracturing and subsequent grain-size-sensitive creep in lower crustal gabbros: evidence for coseismic loading followed by creep during decaying stress in the lower crust? Journal of Geophysical Research: Solid Earth, 120, 3119–3141.

Okudaira, T., Shigematsu, N., Harigane, Y., and Yoshida, K. (2017) Grain size reduction due to fracturing and subsequent grain-size-sensitive creep in a lower crustal shear zone in the presence of a CO_2-bearing fluid. Journal of Structural Geology, 95, 171–187.

O'Neil, J.R., and Taylor, H.P. (1967) The oxygen isotope and cation exchange chemistry of feldspars. American Mineralogist, 52, 1414–1437.

Petley-Ragan, A., Dunkel, K.G., Austrheim, H., Ildefonse, B., and Jamtveit, B. (2018) Microstructural records of earthquakes in the lower crust and associated fluid-driven metamorphism in plagioclase-rich granulites. Journal of Geophysical Research: Solid Earth, 123, 3729–3746.

Plattner, U., Markl, G., and Sherlock, S. (2003) Chemical heterogeneities of Caledonian (?) pseudotachylytes in the Eidsfjord Anorthosite, north Norway. Contributions to Mineralogy and

Petrology, 145, 316–338.

Plümper, O., Botan, A., Los, C., Liu, Y., Malthe-Sørenssen, A., and Jamtveit, B. (2017) Fluid-driven metamorphism of the continental crust governed by nanoscale fluid flow. Nature Geoscience, 10, 685–690.

Putnis, A. (2002) Mineral replacement reactions: from macroscopic observations to microscopic mechanisms. Mineralogical Magazine, 66, 689–708.

Putnis, A. (2015) Transient porosity resulting from fluid–mineral interaction and its consequences. Reviews in Mineralogy and Geochemistry, 80, 1–23.

Ravna, E.K. (2000) Distribution of Fe^{2+} and Mg between coexisting garnet and hornblende in synthetic and natural systems: an empirical calibration of the garnet–hornblende Fe–Mg geothermometer. Lithos, 53, 265–277.

Schmalholz, S.M., and Podladchikov, Y.Y. (2013) Tectonic overpressure in weak crustal-scale shear zones and implications for the exhumation of high-pressure rocks. Geophysical Research Letters, 40, 1984–1988.

Sharp, Z.D., and Moecher, D.P. (1994) O-isotope variations in a porphyroclastic meta-anorthosite: Diffusion effects and false isotherms. American Mineralogist, 79, 951–959.

Soda, Y., and Okudaira, T. (2018) Microstructural evidence for the deep pulverization in a lower crustal meta-anorthosite. Terra Nova, 30, 399–405.

Steltenpohl, M.G., Hames, W.E., and Andresen, A. (2004) The Silurian to Permian history of a metamorphic core complex in Lofoten, northern Scandinavian Caledonides. Tectonics, 23, doi.org/10.1029/2003TC001522.

Steltenpohl, M.G., Moecher, D., Andresen, A., Ball, J., Mager, S., and Hames, W.E. (2011) The Eidsfjord shear zone, Lofoten–Vesterålen, north Norway: An Early Devonian, paleoseismogenic low-angle normal fault. Journal of Structural Geology, 33, 1023–1043.

Svahnberg, H., and Piazolo, S. (2010) The initiation of strain localization in plagioclase-rich rocks: Insights from detailed microstructural analyses. Journal of Structural Geology, 32, 1404–1416.

Wain, A.L., Waters, D.J., and Austrheim, H. (2001) Metastability of granulites and process of eclogitisation in the UHP region of western Norway. Journal of Metamorphic Geology, 19, 609–625.

Wayte, G.J., Worden, R.H., Rubie, D.C., and Droop, G.T.R. (1989) A TEM study of disequilibrium plagioclase breakdown at high pressure: the role of infiltrating fluid.

Contributions to Mineralogy and Petrology, 101, 426–437.

Whitney, D.L., and Evans, B.W. (2010) Abbreviations for names of rock-forming minerals. American Mineralogist, 95, 185–187.

This is a preprint, the final version is subject to change, of the American Mineralogist (MSA)
Cite as Authors (Year) Title. American Mineralogist, in press.
DOI: https://doi.org/10.2138/am-2020-7284

FIGURE CAPTIONS

FIGURE 1. (**a**) Location of the study area in Langøya, Vesterålen, northern Norway. (**b**) Geological map of the Eidsfjord anorthosite complex and the surrounding region (Markl 1998; Okudaira et al. 2017) with the locations of the samples (anorthositic mylonite sample 160730-02 in Fleinnes and sparsely fractured anorthosite sample 170731-02 in Kjørstad) analyzed in this study indicated by pink stars. Yellow stars indicate the sample locations in Okudaira et al. (2017). The topographic contours (dashed lines) are at 200-m intervals.

FIGURE 2. Microstructures in the sparsely fractured anorthosites. (**a**) Coarse-grained (>1 cm) plagioclase and orthopyroxene showing no distinct deformation microstructures such as the formation of small grains at the margins of igneous minerals. Biotite occurs at the rims of orthopyroxene. The opaque mineral (black in the image) is Fe–Ti oxide. Plane-polarized light. (**b**) Mechanical twins and cracks in coarse-grained plagioclase. Mechanical twins comparable to Albite or Pericline laws are terminated or offset by cracks. Arrowheads indicate representative cracks. The enlarged image (lower left) shows fine-grained plagioclase within the cracks. Abbreviations: AT = Albite twin; PT = Pericline twin. Crossed-polarized light (XPL). (**c**) Occurrence of crack-infilling plagioclase. The box

indicates the extent of **d**. XPL. (**d**) Backscattered electron (BSE) image showing the occurrence of lower X_{An}, crack-infilling plagioclase (dark gray), epidote, and apatite along the crack. (**e**) BSE image showing the occurrence of crack-infilling, fine-grained plagioclase with lower X_{An}, epidote, kyanite, and quartz. Broken lines indicate boundaries between the host plagioclase and the cracks. (**f**) Garnet surrounded by tschermakite and biotite. Orthopyroxene is replaced by cummingtonite. Hornblende occurs occasionally with tschermakite.

Figure 3. Histograms showing X_{An} of intact coarse-grained plagioclase and crack-infilling plagioclase in sparsely fractured anorthosites.

FIGURE 4. Microstructures in the anorthositic mylonites. (**a**) Plagioclase grains occur as a recrystallized matrix and porphyroclasts. XPL. (**b**) Plagioclase grains forming the matrix show an equilibrium structure (i.e., a foam structure) and individually have an optically zonal structure. Plagioclase grains labeled with Grain # correspond to the grains on which SIMS oxygen isotope analyses were conducted (see Fig. 7). XPL.

FIGURE 5. Characteristics of the zonal structure in the matrix plagioclase of the anorthositic mylonites. (**a**) Photomicrograph of chemically zoned plagioclase grains. The black box

indicates the extent of the elemental map and EBSD measurement area. XPL. (**b**) Elemental intensity map of Ca. (**c**) Intragranular misorientation map (MTEX toolbox "mis2mean") of the zoned plagioclase grains. Line A–A′ indicates the line profile in (**d**). The scale bar relates to the intragranular misorientation (in degrees) between a given point and the average orientation. (**d**) Line profiles of misorientation angles and X_{An} along line A–A′ in (**c**).

FIGURE 6. Histogram showing X_{An} from the Na-rich cores and Ca-rich rims of chemically zoned matrix plagioclase and porphyroclasts in the anorthositic mylonites. Data for porphyroclasts are multiple-point measurements from five porphyroclasts.

FIGURE 7. $\delta^{18}O_{VSMOW}$ of fine-grained plagioclase in the anorthositic mylonites. (**a**) $\delta^{18}O_{VSMOW}$ vs. X_{An}. The X_{An} values are from the EPMA results from nearby SIMS analysis spots. Error bars show 2 standard errors in each spot measurement. (**b**) $\delta^{18}O_{VSMOW}$ across a single plagioclase grain (Grain 6). The SEM image (inset) shows the measurement spots.

FIGURE 8. Summary of *P–T* estimates for the hydration products in the sparsely fractured anorthosites. KS90, HB94, and R00 represent the results of the thermobarometers developed by Kohn and Spear (1990), Holland and Blundy (1994), and Ravna (2000),

respectively. The gray area labeled O17 represents the *P–T* range obtained by Okudaira et al. (2017). The aluminosilicate phase diagram is from Holdaway (1971).

FIGURE 9. Model for the formation of Na-rich cores and Ca-rich rims in matrix plagioclase grains of anorthositic mylonites. (**a**) Equilibrium phase diagram for plagioclase at low pressure (Carpenter 1994). The field in which *C*-1 + e_1 crystals coexist in the Bøggild miscibility gap of Jin and Xu (2017) is illustrated as a gray area. The 1σ compositional range of the Na-rich cores (X_{An} = 0.26–0.36; blue box) and Ca-rich rims (X_{An} = 0.39–0.45; red box) are also shown. The temperature ranges for the Na-rich cores and Ca-rich rims are assumed to be from 500 to 700 °C. (**b**) Semiquantitative isothermal *P*–X_{An} diagram showing calculated equilibrium phase boundaries for the albite–anorthite pseudobinary system in the presence of pure water from 500 to 800 °C. These are calculated using the data set of Holland and Powell (1998, revised 2002) with excess H_2O. The solution model of Newton et al. (1980) is used for plagioclase. The results of experiments by Goldsmith (1982) and thermodynamic analysis by Wayte et al. (1989) are shown as a dotted curve labeled G82 and gray curves labeled W89, respectively. The 1σ compositional ranges of the Na-rich cores (blue box) and the Ca-rich rims (red box) are also shown. The pressure

This is a preprint, the final version is subject to change, of the American Mineralogist (MSA)
Cite as Authors (Year) Title. American Mineralogist, in press.
DOI: https://doi.org/10.2138/am-2020-7284

ranges for the Na-rich cores and Ca-rich rims are 0.9–1.0 and 0.6–0.7 GPa, respectively.

FIGURE 10. Cartoon showing the development of a mylonite zone at the first- and second-stage fracturing and metamorphism during nearly isothermal decompression. Insets show the microstructural development of each stage. (**a**) Fractures developed in anorthosites at the first-stage higher-*P* fracturing and metamorphism. Metamorphic recrystallization attending an influx of hydrous fluids may be focused on the intensely fractured zone. Plagioclases with X_{An} = ~0.3 were precipitated or replaced. Metamorphic epidote, kyanite, and quartz crystallized at grain boundaries between recrystallized plagioclase grains. (**b**) Fractures developed in anorthosites at the second-stage lower-*P* fracturing and metamorphism. Metamorphic recrystallization attending an infiltration of H_2O-CO_2 fluids was focused on a zone of second stage fracturing, which was overprinted on the fractured and recrystallized zone formed at the first stage. The sparsely fractured anorthosites analyzed in this study essentially escaped from the second-stage metamorphic recrystallization. Plagioclases with X_{An} = ~0.4 were precipitated or replaced. The modal abundances of epidote, kyanite, and quartz would be reduced with the progress of the reaction (1). Scapolite also crystallized at grain boundaries between plagioclase grains.

This is a preprint, the final version is subject to change, of the American Mineralogist (MSA)
Cite as Authors (Year) Title. American Mineralogist, in press.
DOI: https://doi.org/10.2138/am-2020-7284

SUPPLEMENTARY MATERIALS

SUPPLEMENTAL TABLE S1. Oxygen isotopic values for plagioclase in the anorthositic mylonite (sample 160730-02-13b)

SUPPLEMENTAL FIGURE S1. Chemical composition of amphibole grains in the sparsely fractured anorthosite (sample 170731-02). (**a**) Si vs. Mg / (Mg + Fe^{2+}). (**b**) $(Na + K)_A$ vs. ^{IV}Al. Amphibole classification follows that of Leake et al. (1997).

SUPPLEMENTAL FIGURE S2. Ternary Mg–Fe–Ca diagram showing the composition of garnet in the sparsely fractured anorthosite (sample 170731-02).

SUPPLEMENTAL FIGURE S3. Backscattered electron image of the boundary zone between Na-rich core and Ca-rich rim in plagioclase which is the same as the grain for line profiles in Fig. 5c. There is no microscale porosity in the Ca-rich rim. Dashed line denotes boundary between Na-rich core and Ca-rich rim in plagioclase.

This is a preprint, the final version is subject to change, of the American Mineralogist (MSA)
Cite as Authors (Year) Title. American Mineralogist, in press.
DOI: https://doi.org/10.2138/am-2020-7284

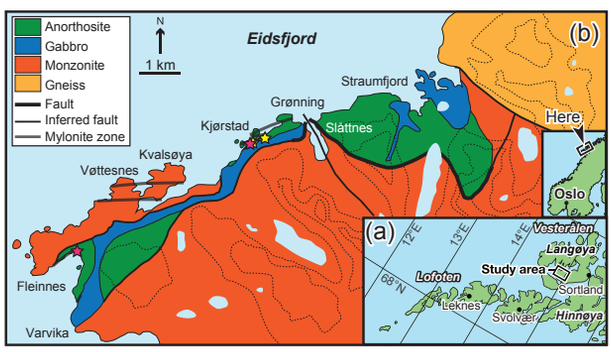

Figure 1

This is a preprint, the final version is subject to change, of the American Mineralogist (MSA)
Cite as Authors (Year) Title. American Mineralogist, in press.
DOI: https://doi.org/10.2138/am-2020-7284

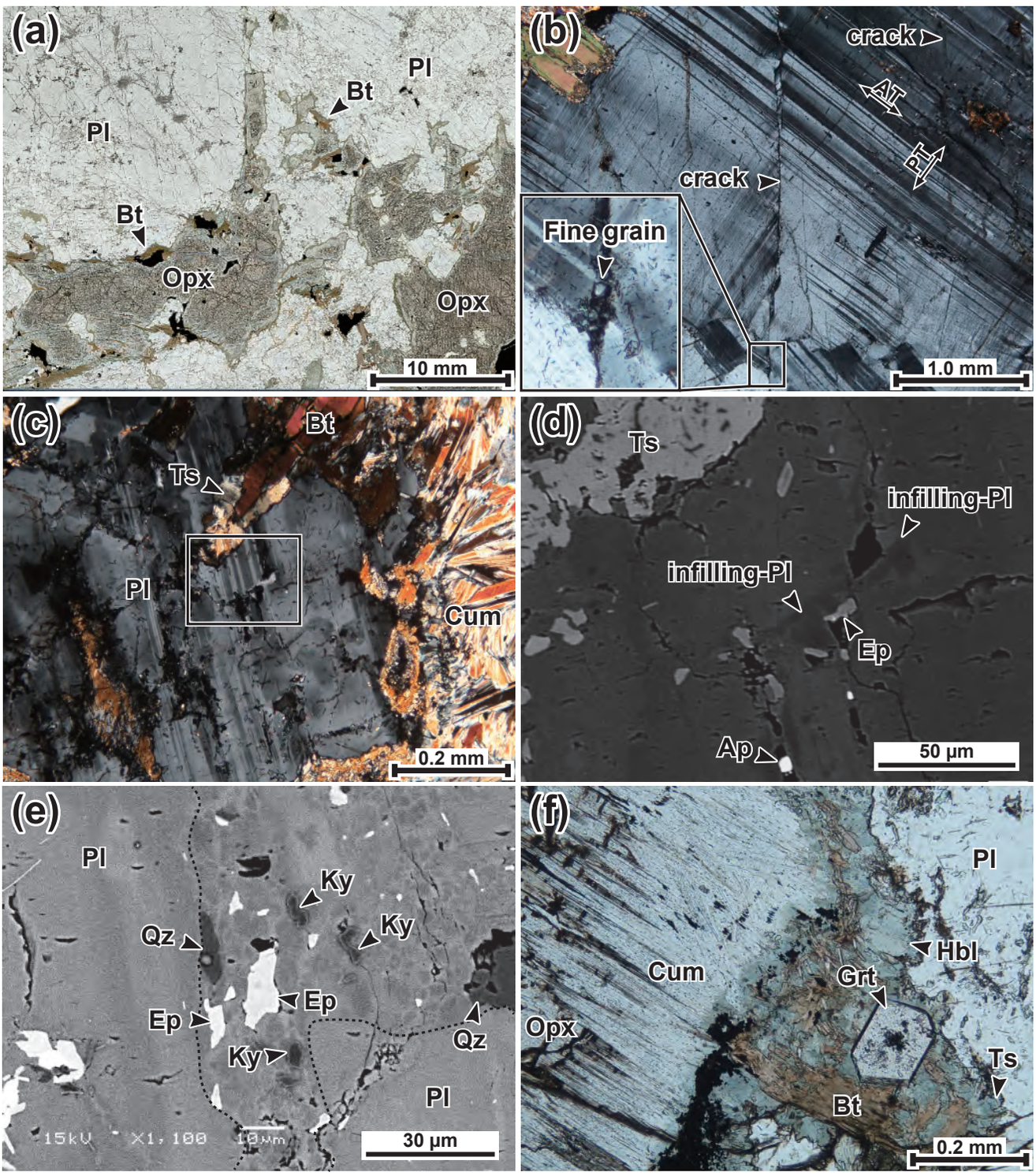

Figure 2

This is a preprint, the final version is subject to change, of the American Mineralogist (MSA)
Cite as Authors (Year) Title. American Mineralogist, in press.
DOI: https://doi.org/10.2138/am-2020-7284

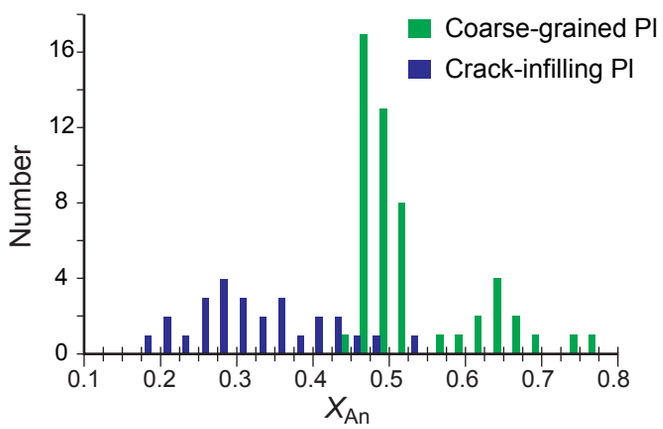

Figure 3

This is a preprint, the final version is subject to change, of the American Mineralogist (MSA)
Cite as Authors (Year) Title. American Mineralogist, in press.
DOI: https://doi.org/10.2138/am-2020-7284

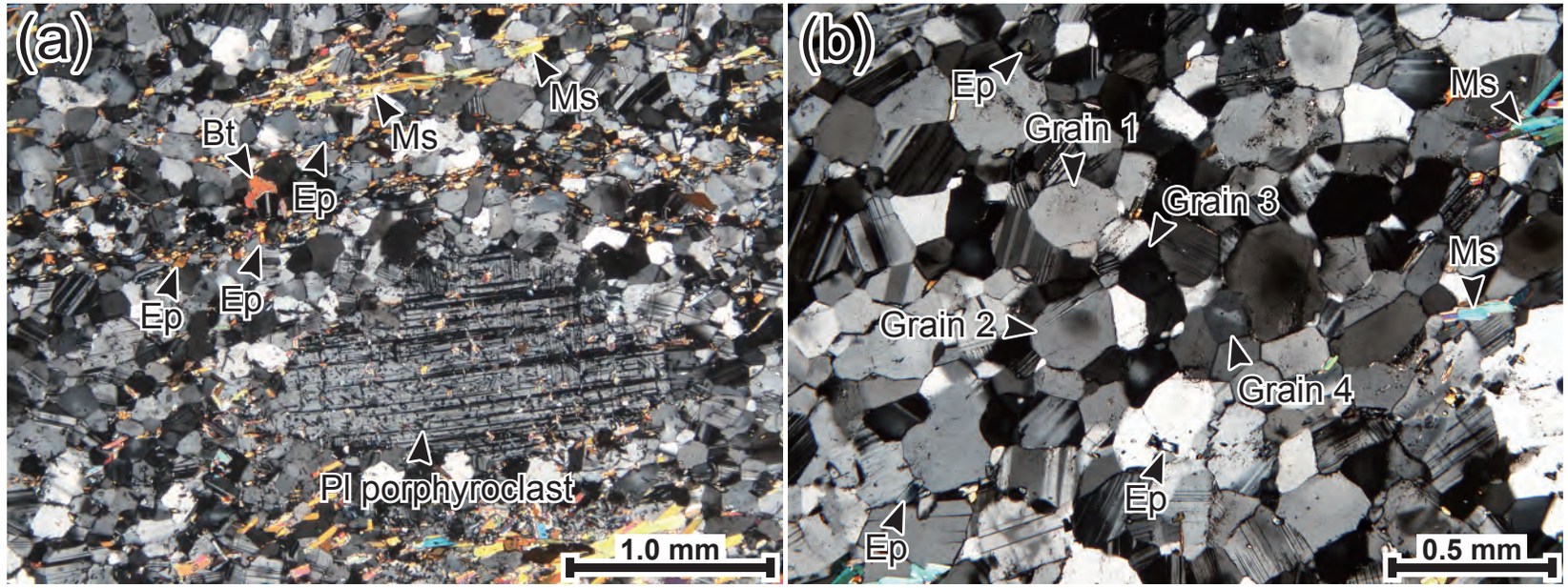

Figure 4

This is a preprint, the final version is subject to change, of the American Mineralogist (MSA)
Cite as Authors (Year) Title. American Mineralogist, in press.
DOI: https://doi.org/10.2138/am-2020-7284

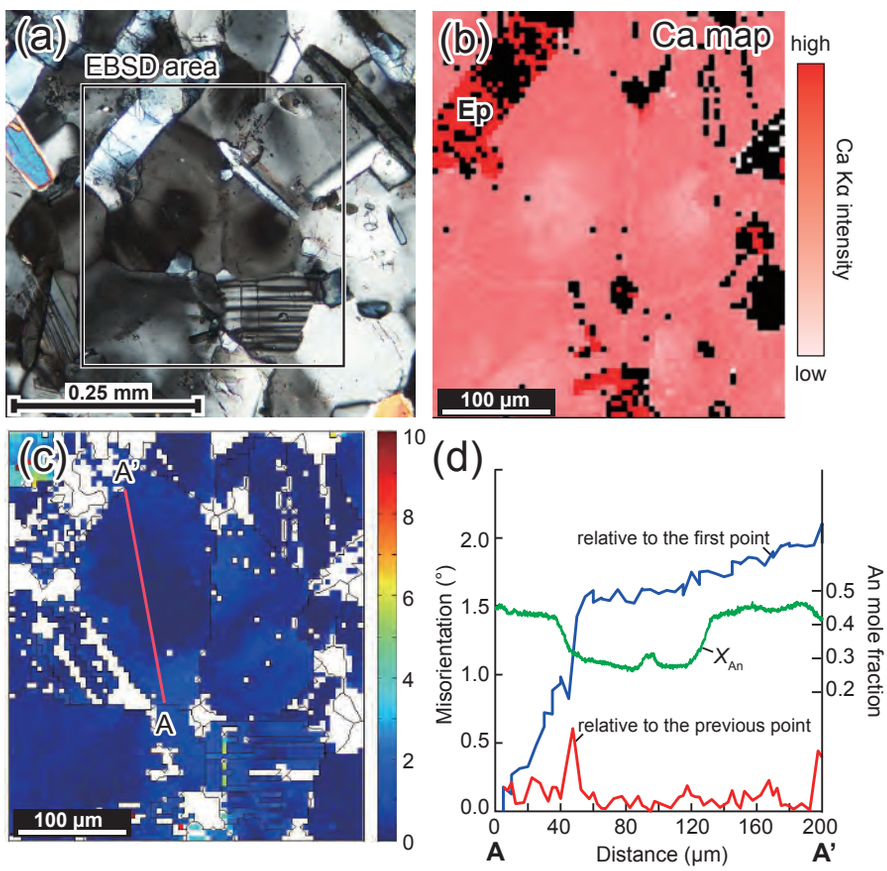

Figure 5

This is a preprint, the final version is subject to change, of the American Mineralogist (MSA)
Cite as Authors (Year) Title. American Mineralogist, in press.
DOI: https://doi.org/10.2138/am-2020-7284

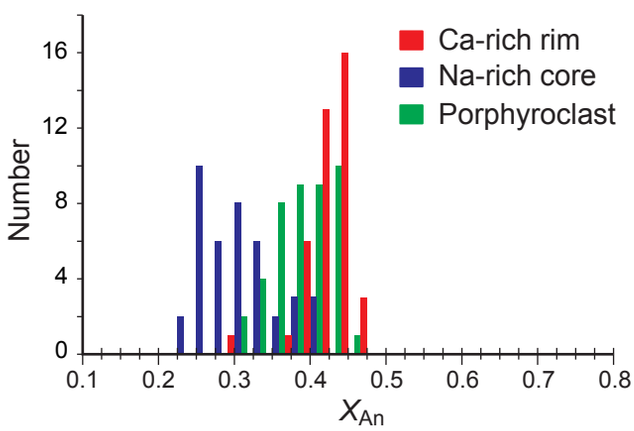

Figure 6

This is a preprint, the final version is subject to change, of the American Mineralogist (MSA)
Cite as Authors (Year) Title. American Mineralogist, in press.
DOI: https://doi.org/10.2138/am-2020-7284

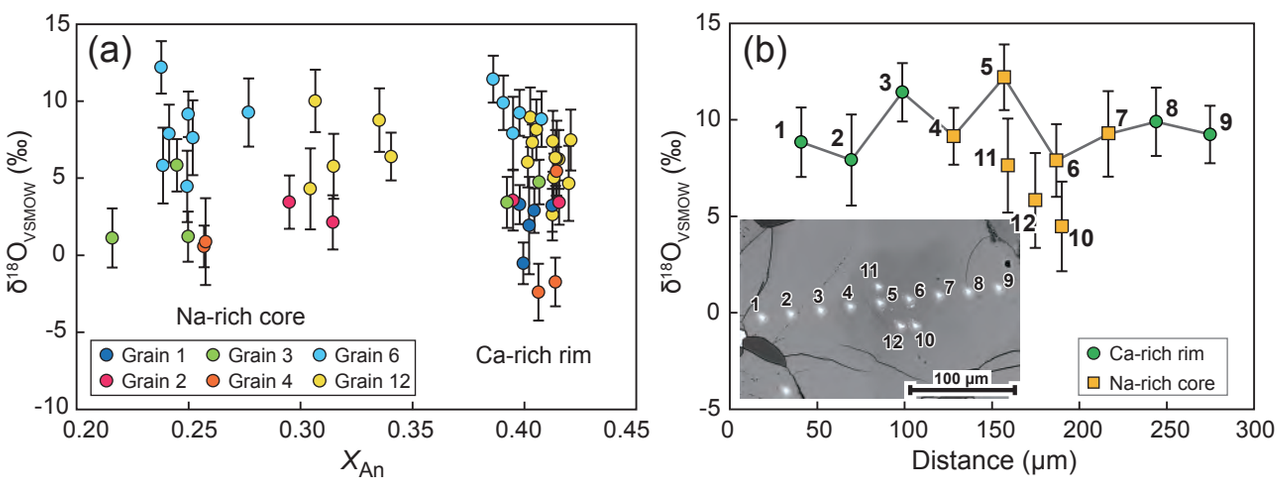

Figure 7

This is a preprint, the final version is subject to change, of the American Mineralogist (MSA)
Cite as Authors (Year) Title. American Mineralogist, in press.
DOI: https://doi.org/10.2138/am-2020-7284

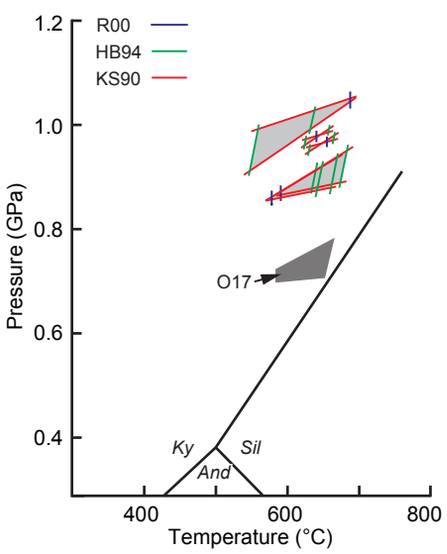

Figure 8

This is a preprint, the final version is subject to change, of the American Mineralogist (MSA)
Cite as Authors (Year) Title. American Mineralogist, in press.
DOI: https://doi.org/10.2138/am-2020-7284

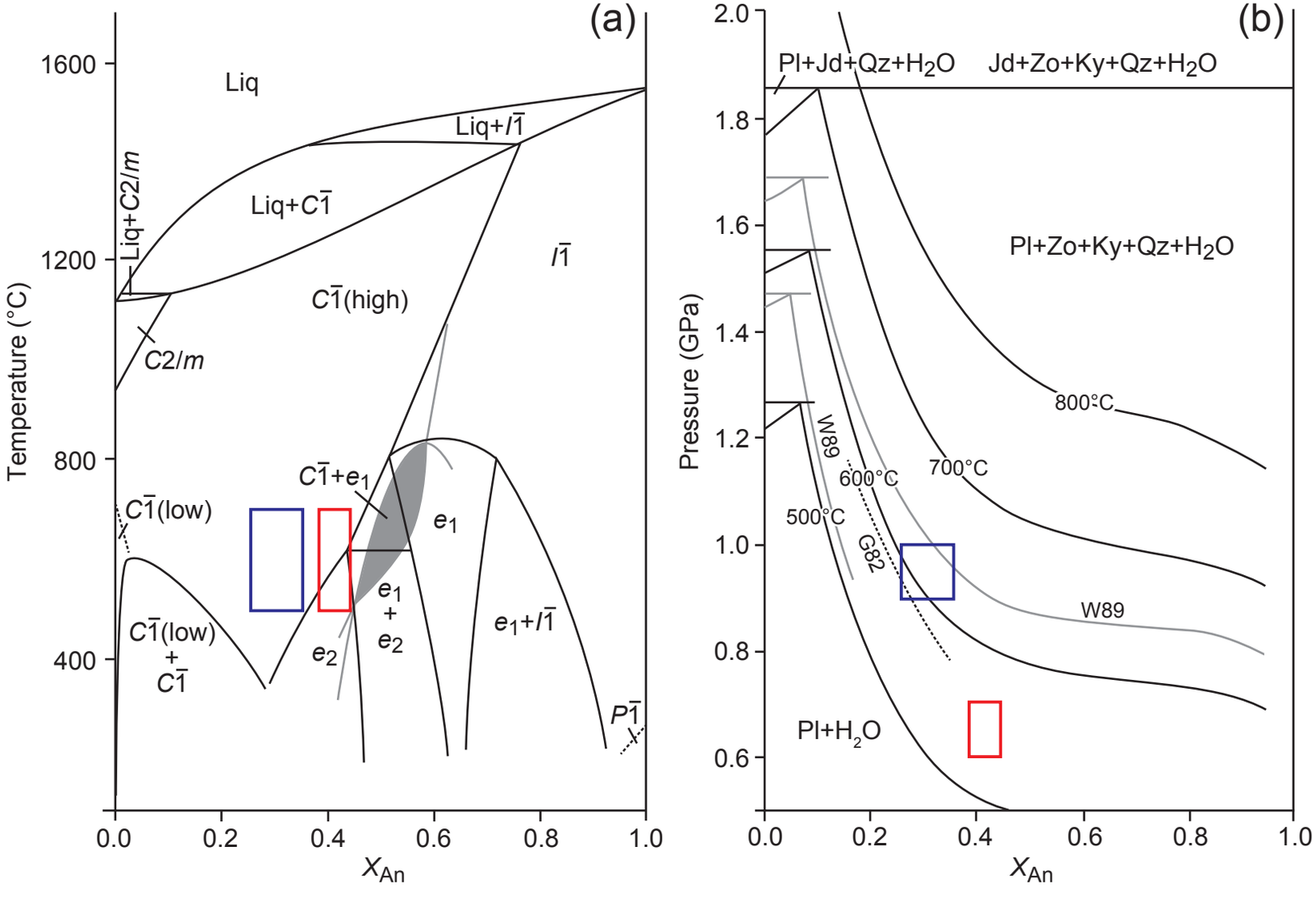

Figure 9

This is a preprint, the final version is subject to change, of the American Mineralogist (MSA)
Cite as Authors (Year) Title. American Mineralogist, in press.
DOI: https://doi.org/10.2138/am-2020-7284

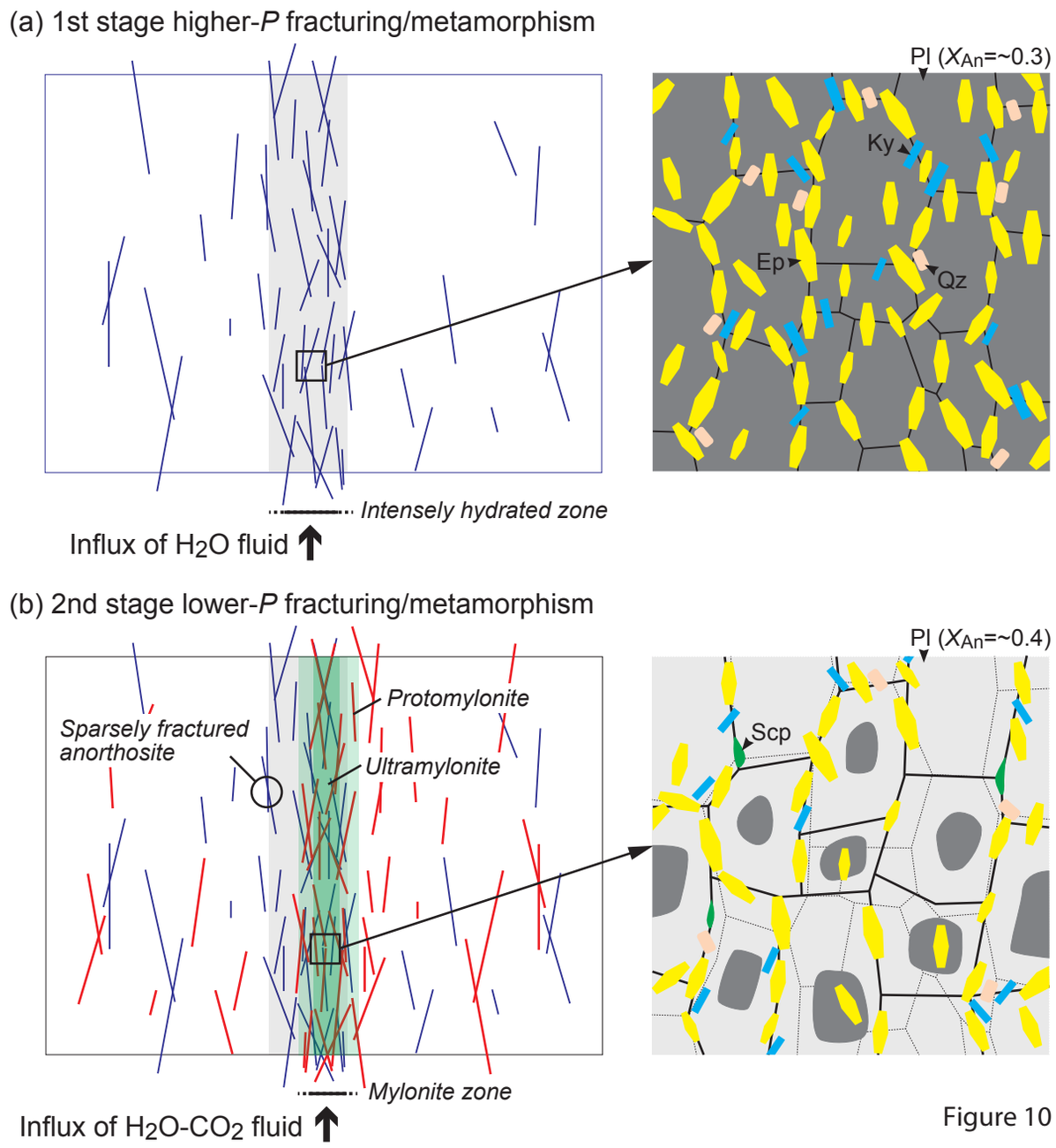

Figure 10

This is a preprint, the final version is subject to change, of the American Mineralogist (MSA)
Cite as Authors (Year) Title. American Mineralogist, in press.
DOI: https://doi.org/10.2138/am-2020-7284

TABLE 1. The results of *P–T* estimates and mineral chemistry of plagioclase (Pl), amphibole (Amp) and garnet (Grt) in the sparsely fractured anorthosite (sample 170731-02) used for *P–T* calculations

Pair	#1			#2			#3			#4			#5		
	Pl	Amp	Grt	Pl	Amp	Grt	Pl	Amp	Grt	Pl	Amp	Grt	Pl	Amp	Grt
(wt%)															
SiO_2	64.54	41.63	39.42	63.53	41.50	39.10	60.06	41.27	39.45	61.35	41.39	39.17	62.51	41.61	39.46
TiO_2	0.01	0.36	0.03	–	0.57	0.06	0.01	0.20	0.03	0.01	0.62	0.03	–	0.47	0.01
Al_2O_3	23.44	16.80	21.41	23.89	16.32	21.42	24.85	17.12	21.71	24.24	16.94	21.39	24.13	16.96	21.59
FeO	0.08	14.32	26.70	0.02	16.21	27.87	0.01	14.80	26.66	0.03	14.39	27.25	0.01	15.85	27.72
MnO	–	0.19	2.50	0.01	0.10	1.63	0.02	0.13	2.06	0.01	0.14	1.46	–	0.09	1.57
MgO	–	8.85	4.60	–	8.56	4.38	0.00	9.38	5.03	–	9.51	5.77	0.01	8.83	5.07
CaO	4.66	12.38	5.78	5.27	11.75	6.00	6.66	11.82	6.09	6.13	11.11	4.86	5.62	11.69	5.89
Na_2O	9.11	1.11	0.01	8.54	1.29	0.01	7.16	1.22	0.08	7.98	1.45	–	8.20	1.34	0.02
K_2O	0.16	1.09	–	0.14	1.11	0.01	0.13	0.77	0.00	0.10	0.67	–	0.13	0.96	0.00
O	8	23	12	8	23	12	8	23	12	8	23	12	8	23	12
Si	2.798	6.222	3.067	2.772	6.188	3.051	2.696	6.118	3.045	2.727	6.149	3.052	2.752	6.148	3.045
Ti	0.000	0.040	0.002	–	0.064	0.004	0.000	0.022	0.002	0.000	0.069	0.002	–	0.053	0.001
Al	1.197	2.959	1.963	1.228	2.867	1.969	1.314	2.991	1.975	1.270	2.965	1.964	1.252	2.954	1.963
Fe^{2+}	0.003	1.789	1.737	0.001	2.020	1.818	0.000	1.835	1.721	0.001	1.788	1.775	0.000	1.959	1.789
Mn	–	0.024	0.164	0.000	0.012	0.108	0.001	0.017	0.134	0.001	0.018	0.096	–	0.011	0.103
Mg	–	1.971	0.533	–	1.903	0.509	0.000	2.074	0.579	–	2.105	0.670	0.000	1.945	0.583
Ca	0.217	1.983	0.482	0.246	1.876	0.501	0.320	1.878	0.503	0.292	1.769	0.406	0.265	1.851	0.487
Na	0.766	0.322	0.001	0.723	0.372	0.001	0.623	0.351	0.012	0.687	0.418	–	0.700	0.385	0.002

This is a preprint, the final version is subject to change, of the American Mineralogist (MSA)
Cite as Authors (Year) Title. American Mineralogist, in press.
DOI: https://doi.org/10.2138/am-2020-7284

K	0.009	0.209	–	0.008	0.211	0.001	0.008	0.145	0.000	0.005	0.126	–	0.007	0.181	0.000
X_{An} [a]	0.22			0.25			0.34			0.30			0.27		
Amphibole formula [b]															
^{IV}Al		1.778			1.812			1.882			1.851			1.852	
^{VI}Al		1.180			1.054			1.110			1.114			1.101	
Fe^{3+}		0.014			0.187			0.362			0.328			0.241	
Fe^{2+}		1.775			1.833			1.473			1.460			1.718	
Na_B		0.013			0.070			0.065			0.137			0.080	
$(Na + K)_A$		0.517			0.513			0.431			0.407			0.485	
X_{Mg} [c]		0.53	0.23		0.51	0.22		0.58	0.25		0.59	0.27		0.53	0.25
Mole fraction of end-members in garnet [d]															
X_{Alm}			0.60			0.62			0.59			0.60			0.60
X_{Sps}			0.06			0.04			0.05			0.03			0.03
X_{Prp}			0.18			0.17			0.20			0.23			0.20
X_{Grs}			0.17			0.17			0.17			0.14			0.16
Temperature (°C) at 900 MPa [e]															
HB94	616/545			645/615			675/637			663/645			653/622		
R00	687			640			590			577			655		

This is a preprint, the final version is subject to change, of the American Mineralogist (MSA)
Cite as Authors (Year) Title. American Mineralogist, in press.
DOI: https://doi.org/10.2138/am-2020-7284

Pressure (MPa) at 600 °C [f]					
KS90	1011/962	963/939	868/881	856/880	947/922

[a] X_{An} = Ca / (Ca + Na + K)

[b] Amphibole formula are of average of the maximum and minimum estimated amount of ferric iron (Leake et al. 1997)

[c] X_{Mg} = Mg / (Fe^{2+} + Mg)

[d] Mole fraction of end-members in garnet: X_{Alm} = Fe^{2+} / (Fe^{2+} + Mn + Mg + Ca), X_{Sps} = Mn / (Fe^{2+} + Mn + Mg + Ca), X_{Prp} = Mg / (Fe^{2+} + Mn + Mg + Ca), X_{Grs} = Ca / (Fe^{2+} + Mn + Mg + Ca)

[e] HB94 Holland and Blundy (1994) with or without quartz, R00 Ravna (2000)

[f] KS90 Kohn and Spear (1990) with Mg end-member or Fe end-member